

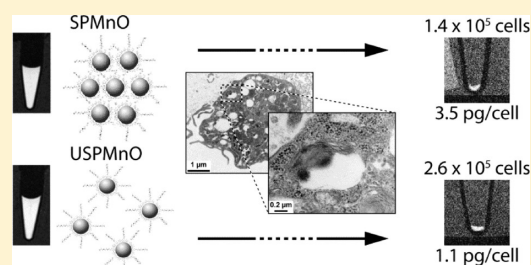
MnO-Labeled Cells: Positive Contrast Enhancement in MRI

Mathieu Létourneau,^{†,‡,§} Mélanie Tremblay,^{†,‡,§} Luc Faucher,^{‡,§} Dario Rojas,^{‡,§} Pascale Chevallier,[‡] Yves Gossuin,^{||} Jean Lagueux,[‡] and Marc-André Fortin^{*,‡,§}[‡]Axe métabolisme, santé vasculaire et rénale, Centre de recherche du Centre hospitalier universitaire de Québec (AMSVR-CRCHUQ), 10 rue de l'Espinaie, Québec, QC G1L 3L5, Canada[§]Centre de recherche sur les matériaux avancés (CERMA) and Département de génie des mines, de la métallurgie et des matériaux, Université Laval, Québec, QC G1V 0A6, Canada^{||}Service de physique expérimentale et biologique, Université de Mons, 20, Place du Parc, Mons, Belgium

S Supporting Information

ABSTRACT: Manganese oxide (MnO) nanoparticles have been suggested as a promising “positive” MRI contrast agent for cellular and molecular studies. Mn-based contrast agents could enable T_1 -weighted quantitative cell tracking procedures in vivo based on signal enhancement. In this study, ultrasmall MnO particles were synthesized and coated with thiolated molecules (DMSA) and polyethylene glycol (PEG) to allow enhanced cell labeling properties and colloidal stability. This coating allowed the fabrication of individual ultrasmall nanoparticles of MnO (USPMnO) as well as of nanoaggregates of the same material (SPMnO). Particle size was measured by TEM and DLS. Physico-chemical properties

were characterized by XPS and FTIR. The relaxometric properties of these aqueous suspensions were measured at various magnetic fields. The suspensions provided strong positive contrast enhancement in T_1 -weighted imaging due to high longitudinal relaxivities (r_1) and low r_2/r_1 ratios (USPMnO: $r_1 = 3.4 \pm 0.1 \text{ mM}^{-1}\text{s}^{-1}$, $r_2/r_1 = 3.2$; SPMnO: $r_1 = 17.0 \pm 0.5 \text{ mM}^{-1}\text{s}^{-1}$, $r_2/r_1 = 4.0$, at 1.41T). HT-1080 cancer cells incubated with the contrast agents were clearly visualized in MRI for Mn contents $>1.1 \text{ pg/cell}$. The viability of cells was not affected, contrarily to cells labeled with an equivalent concentration of Mn^{2+} ions. A higher signal per cell was found for SPMnO-labeled compared with USPMnO-labeled cells, due to the higher relaxometric properties of the agglomerates. As a result, the “positive” signal enhancement effect is not significantly affected upon agglomeration of MnO particles in endosomes. This is a major requirement in the development of reliable cell tracking procedures using T_1 -weighted imaging sequences. This study confirms the potential of SPMnO and USPMnO to establish more quantitative cell tracking procedures with MRI.



■ INTRODUCTION

Tracking the distribution of injected cells in vivo has become one of the most important applications of preclinical magnetic resonance imaging (MRI). New therapies based on the injection of stem and progenitor cells, of dendritic and T cells, as well as on Langerhans islet implantation,¹ require the development of dedicated MRI procedures and contrast agents to assess the local presence of injected cells in vivo. The development of more quantitative procedures to demonstrate the homing of cells into host tissues is a crucial aspect of this research area.² MRI is the imaging modality of choice for such an application, because it enables whole-body imaging without the use of ionizing radiation, at a near-microscopic resolution, and excellent soft-tissue contrast. Prior to injection and visualization, cells are labeled with magnetic contrast agents (CAs) in order to appear contrast-enhanced in MR images.

Most cell tracking studies in MRI are performed by using, as a CA, superparamagnetic iron oxide either in the form of nanoagglomerates (SPIO; 100–150 nm) or as individual nanoparticles (USPIO; 20–40 nm).^{2–5} Such products, referred to as “negative” CAs, have been widely used in cell tracking

procedures because of their capacity to shorten T_2 and to generate T_2^* effects.^{3,6–10} Although iron oxide-labeled cells can be sensitively detected with negative iron oxide particles, the difficulty of correlating the signal intensity with the amount of labeled cells accumulated or injected in a specific site is a limitation of T_2/T_2^* “negative” CAs (i.e., USPIO and SPIO). In MR images, the large magnetic susceptibility of these particles affects an area that extends far beyond the volume of the labeled cells.^{11–13} Finally, voids generated by the agent cannot be distinguished from other sources of signal loss (e.g., blood clots, tissue–air interfaces, calcification areas).¹⁴

The performance (i.e., contrast enhancement, biodistribution, and bioretention) of SPIO and USPIO as CAs mainly depends on their size and molecular coating. After intravenous administration, SPIO are cleared from the blood within minutes, and they rapidly accumulate in the liver and in the spleen through the mononuclear phagocytic system.¹⁵ On the

Received: April 6, 2012

Revised: September 25, 2012

Published: October 3, 2012

other hand, smaller USPIO can transmigrate the capillary walls, as well as being retained in the blood for longer times.¹⁶ A significant fraction of USPIO can accumulate in the bone marrow and in the lymph nodes. Whereas individual USPIO provide transversal relaxivities (r_2) in the range 33–89 mM⁻¹s⁻¹, with relaxometric ratios (r_2/r_1) from 2.39 to 6.56, SPIO particles have r_2 values systematically higher than 100, with r_2/r_1 well above a value of 10 at clinical magnetic field strengths.² Therefore, aggregation is expected to influence the relaxometric properties of magnetic nanoparticle suspensions and, in the case of iron oxide particles, result in significant susceptibility artifacts in MR images.

“Positive” MRI CAs have been suggested as a promising alternative to USPIO and SPIO for a variety of cell transplantation and tracking procedures, particularly for applications requiring the visualization of local accumulations in the order of several thousand cells.^{17–22} Manganese (Mn) has been used as a “positive” CA since the inception of MRI.²³ MnCl₂ has been successfully used to investigate neurological tissues and also as a “positive” CA for cell tracking studies.^{24,25} Products based on Mn²⁺ could enable more quantitative cell tracking studies relying on the precise measurement of local contrast enhancement effects, and this at lower toxicity risks than with Gd³⁺-based products. Mn-based CAs could improve the delineation of fine anatomical structures around the site of cell implantation, or cell accumulation, which would be a key advantage in cell tracking procedures.^{26–28} Positive CAs are defined by their high longitudinal relaxivities ($r_1 > 1$ mM⁻¹s⁻¹) and relatively low r_2/r_1 ratios (<5). When such particles are suspended in aqueous medium, they preferentially decrease the longitudinal relaxation time of ¹H protons, resulting in a significant signal increase. They are not expected to cause magnetic susceptibility artifacts.

Ultrasmall manganese oxide nanoparticles (MnO) have recently been suggested as efficient “positive” CAs.²⁹ They concentrate thousands of Mn atoms per CA unit, the highest density for Mn-based CAs. Although the first reported MnO suspensions did not provide optimal r_2/r_1 ratios for T₁-weighted MRI, recent advances in nanoparticle coating and ligand exchange (e.g., polyethylene glycol: PEG) have greatly improved their relaxometric properties.^{30,31} The potential of MnO nanoparticles for cell labeling in T₁-weighted and T₁-mapping imaging has been demonstrated by Gilad et al.²¹ Morphologically, MnO nanoparticles systems are very similar to SPIO and USPIO. They both are made of an ultrasmall crystalline oxide core, surrounded by a coating of biocompatible molecules. In the present study, we demonstrate the possibility to synthesize both suspensions of individual particles and agglomerates of MnO cores. It is therefore of prime importance to measure the influence of agglomeration on the relaxometric properties of such suspensions. This is particularly relevant in the context of cell tracking procedures, because small particles of metal oxide ingested by cells are expected to agglomerate into the endosomes. MnO contrast agents maintaining relatively constant and moderate relaxometric ratios (r_2/r_1) upon agglomeration could represent a significant advantage for T₁-weighted cell tracking procedures.

In the present study, MnO nanoparticles (8.4 nm diam.) were synthesized and then coated with dimercaptosuccinic acid (DMSA) and polyethylene glycol (PEG) to generate small particles of manganese oxide (SPMnO). DMSA is a low toxicity biocompatible molecule. As a ligand, it promotes the cell internalization of iron oxide nanoparticles, while preserving cell

viability.^{32–35} PEG is a biocompatible, nonimmunogenic molecule enhancing the steric repulsion of colloids in biological media.³⁶ Then, by modulating the pH of SPMnO suspensions, disulfide bridges binding the nanocrystals can be cleaved, and this strategy was used in the present study to generate suspensions of individual, ultrasmall DMSA-PEG-coated MnO particles (USPMnO). Core size was characterized by transmission electron microscopy (TEM) and the hydrodynamic diameter measured by dynamic light scattering (DLS). The physicochemical properties of the particles were analyzed by X-ray photoelectron spectroscopy (XPS) and attenuated total reflectance Fourier transform infrared spectroscopy (ATR-FTIR). To quantify their relaxometric performance and to measure the influence of aggregation on contrast enhancement properties, the relaxation times (T_1 , T_2) were measured at different magnetic field strengths. As a cell model to study positive contrast enhancement phenomena, a robust cancer cell line (HT-1080) was used, allowing seeding at reproducible cell densities, fast adhesion, and duplication rates, rapidity of cell growth, limited possibility of multiple phenotypes when reaching confluence, and cell harvest efficiency. The cells were then labeled with the particle suspensions (SPMnO, USPMnO), and the amount of Mn internalized in the cells was quantified. Finally, the cell pellets were imaged in MRI, followed by integration of their signal and normalization with respect to the amount of cells and Mn contents per pellet.

■ MATERIALS AND METHODS

a. MnO Nanocrystal Synthesis. Ultrasmall MnO nanocrystals were prepared by the thermal decomposition technique, which produces narrow particle size distributions of mean diameters in the range 5–20 nm.^{29,37} Unless specified, all chemicals were from Sigma-Aldrich (synthesis grade ~99%). Nanopure water was produced by a Barnstead ultrapure water system (18.2 MΩ·cm). The particles were synthesized as follows: 2.0 g of Mn(NO₃)₂·xH₂O (99.99%) and 6.8 g of Na-oleate were dissolved in 160 mL of ethanol, nanopure water, and *n*-hexane (1:1:2 v/v) and refluxed at 70 °C for 29 h. Thus-formed Mn-oleate complex was decanted and washed twice with 20 mL of nanopure water. The solution was vacuum-dried for at least 24 h. For the decomposition step, 2.39 g of the Mn-(oleate)₂ wax was dissolved in 40 mL of hexadecene (59.8 mg/mL) and sonicated for 2 h at 40 °C. The solution was heated under argon flux to the boiling point of the solvent (5.0 °C/min) and kept under constant stirring at 280–282 °C for 3 min. Then, the suspension was rapidly cooled to 10 °C and transferred to 50 mL centrifugation tubes (20 mL per tube). Ethanol was added to fill each tube up to 45 mL, followed by mixing and sonication for 5 min. The tubes were centrifuged (1600g, 10 °C, 20 min) and the supernatant was discarded. A total of 5 mL of acetone was added to each tube, followed by vortexing, sonication, and by an additional centrifugation cycle (1600g, 10 °C, 10 min). This step was repeated twice. Then, 10 mL of cyclohexane were added in each tube to redisperse the particles, followed by centrifugation (1600g, 20 °C, 30 min). The supernatant was collected, transferred to a 50 mL beaker, dried overnight, and weighted. This product is referred to as MnO-oleate. Nanoparticles of core size included in the range 6.6–12.7 nm were generated using variations of this main synthesis technique (as described in the Supporting Information [SI]).

b. MnO Nanocrystal Analysis (DLS, TEM, XRD). The hydrodynamic diameter of MnO-oleate nanoparticles sus-

pended in chloroform (10 mg/mL) was assessed by DLS (Malvern Zetasizer 173°). Monodisperse particle suspensions with polydispersity index (PDI) < 0.6 were selected for further coating procedures and relaxometric characterization. Drops (3 μ L) of the suspensions were dried on carbon-coated copper grids (Canemco-Marivac, Lakefield, Canada) and imaged by TEM (Jeol-1230, 120 keV). Then, the ImageJ software particle size analysis tool was used to measure the size distribution of the oxide cores on at least 130 particles for each product.³⁸ The crystal structure of MnO particles was assessed both by electron diffraction (with TEM, Jeol-1230, 120 keV) and by X-ray diffraction [XRD; D5000 Siemens (Montreal, QC, Canada), $K\alpha$ Cu (0.15418 nm), 20 mA and 40 kV, using 0.05° 2 θ step, 9.6 s step time].

c. Ligand Exchange (with DMSA and PEG). *DMSA coating:* 30 mg DMSA (*meso*-2,3-dimercaptosuccinic acid, >98%) and 50 μ L of triethylamine (99%) were added to 3 mL of dimethyl sulfoxide (DMSO, >99.7%). Then, 30 mg of MnO-oleate in 3 mL of chloroform were added, followed by vigorous vortexing. The suspensions were transferred into polyethylene tubes and incubated 1 h at 60 °C under constant agitation. After incubation, the products were centrifuged (1600g, 10 °C, 7 min) and the supernatant was discarded. Ethanol (5 mL) was added to the particles, followed by 2 min of sonication and centrifugation (1600g, 10 °C, 7 min). The supernatant was discarded and the procedure was repeated twice with ethanol and twice with acetone (5 mL, 30 min centrifugation each time). Finally, the particles were vacuum-dried and stored at 4 °C for further manipulations. DMSA-covered products are referred to as “MnO–DMSA”. *DMSA-PEG coating:* same procedure as for DMSA coating, except that 5 mg of NH₂-PEG-SH (MW: 5000, Laysan-Bio, Alabama) were added to DMSA and triethylamine in DMSO. DMSA-PEG-covered products are referred to as “MnO–DMSA–PEG”.

d. Preparation of SPMnO (Nanoagglomerates) and USPMnO (Individualized Particles). *SPMnO:* MnO–DMSA and MnO–DMSA–PEG particles were suspended in ultrapure water (1 mg/mL) followed by vigorous vortexing, sonication (30 min), and dialyzed (6 h, ultrapure water pH 6; membrane pore size: 25000 MW; Spectra/Por #6, Rancho Dominguez, CA). The water was changed twice and the sample-to-volume ratio was kept to at least 1:2000. After dialysis, the samples were centrifuged (500g, 5 min) to eliminate large agglomerates, and the supernatant was collected for further analysis. These particles are referred to as “SPMnO”. *USPMnO:* Same protocol as for SPMnO, except that, prior to dialysis, the pH of suspensions was adjusted to 10 by adding NaOH (0.3 M; >99.998%). Disulfide bridges are dissociated thereby, leading to the individualization of MnO particles. This suspension was then vigorously vortexed, sonicated (30 min), dialyzed against ultrapure water pH 6, and centrifuged (3000g, 30 min), and the supernatant was collected. These particles are referred to as “USPMnO”.

e. Hydrodynamic Diameter, Colloidal Stability, and Elemental Analysis. DLS was performed on SPMnO and USPMnO aqueous suspensions to measure the hydrodynamic size of the particles. Then, the suspensions were adjusted to 154 mM of NaCl, and the hydrodynamic diameter was measured again at 2 h and then at 4 and 7 days. The zeta potential measurements were performed on USPMnO at pH from 5 to 9. Due to the possibility of dissociating disulfide bridges at acidic pH, the zeta potential of SPMnO was only assessed at near neutral pH (6.5) with a zeta potentiometer

(Malvern Zetasizer ZS). Finally, samples of each suspension were digested at 110 °C in HNO₃ (trace metal, Fisher Scientific A509–500) and with H₂O₂ (30%, Sigma Aldrich 95321) until the suspension turned clear and transparent. Mn concentration was measured by graphite furnace atomic absorption spectroscopy (GF-AAS; Perkin-Elmer Analyst 800).

f. Physico-Chemical Surface Analysis (FTIR and XPS). USPMnO and SPMnO with both coatings (MnO–DMSA and MnO–DMSA–PEG) were analyzed by ATR-FTIR (Nicolet Magna 550, Thermo-Nicolet, Madison, WI, USA), equipped with a deuterated triglycine sulfate (DTGS) detector and a Ge-coated KBr beam splitter. The particles were also characterized by XPS (PHI 5600-ci spectrometer, Physical Electronics U.S.A., MN, U.S.A.). For this, suspensions were dried on flat silicon substrates and analyzed using a monochromatic aluminum X-ray source for survey spectra (0–1400 eV) at 300 W, while high resolution spectra were obtained by using a standard magnesium X-ray source (1253.6 eV), also at 300 W. For neither analyses was charge neutralization applied. The detection was performed at 45° with respect to the surface normal and the analyzed area was 0.005 cm². The spectrometer work function was adjusted to give 285.0 eV for the main C (1s) peak. Curve fittings for both the survey and the high-resolution C (1s) peaks were determined by means of least-squares using a Shirley background subtraction.

g. Relaxometric Analysis. *¹H relaxometry:* Dilutions of dialyzed USPMnO and SPMnO aqueous suspensions (MnO–DMSA, MnO–DMSA–PEG) were prepared with ultrapure water (100, 50 (1:2), 25 (1:4), and 10% (1:10) v/v) and distributed in NMR tubes or capillaries for analysis at 20, 60, and 300 MHz (corresponding to 0.47, 1.41, and 7.0 T). At each magnetic field strength, longitudinal and transversal relaxation times (T_1 and T_2) were measured at 20 and 37 °C by using Bruker MiniSpec relaxometers (20 and 60 mq) and a Bruker AMX300 spectrometer (300 MHz). Relaxation rates ($1/T_1$ and $1/T_2$) were plotted against Mn concentration values, and relaxivities (r_1 and r_2) were obtained by applying a linear regression of this plot. To identify the proton relaxation mechanism (diffusion or exchange) in water suspensions, aqueous samples were diluted with methanol (50% v/v). T_1 and T_2 relaxation times were monitored at 60 MHz and fitted with mono or biexponential curves.³⁹ *NMRD profiles:* Longitudinal relaxivities (r_1) were measured on 100% v/v suspensions from 0.02 to 40 MHz with a Stellar fast field cycling relaxometer (Mede, Italy) at 5 and 37 °C using 600 μ L of nanoparticle suspension.

h. MRI of CA Suspensions. Samples of USPMnO and SPMnO suspensions were imaged with a clinical 1.5 T GE Signa scanner. The samples were placed in a bowl of nanopure water, and introduced in a head coil. A T_1 -weighted spin echo sequence was used with the following parameters: TE/TR: 10/400 ms; α = 90°; FOV: 13 cm; 1.0 mm slices, 256 \times 256; 4 excitations.

i. Cell Culture. HT-1080 human fibrosarcoma cells were maintained in Dulbecco's modified Eagle medium (DMEM) supplemented with D-glucose (4.5 g/L), L-glutamine, sodium pyruvate (110 mg/L), 10% inactive fetal bovine solution (FBS), and 1% streptomycin-penicillin (all from GIBCO).²⁰ Cells were plated in six-well dishes at 5 \times 10⁵ cells/well in 2 mL of complete DMEM and incubated at 37 °C in humidified 95% air/5% CO₂ for 18 h, until they reached ~80% confluence. Prior to incubation with CA, the cells were rinsed three times with 0.5 mL of serum-free DMEM.

j. Cell Labeling Study. Stock solutions of CAs were adjusted to provide the same longitudinal relaxation time ($T_1 = 80$ ms). The preparation of Mn isoconcentrated solutions would have required just-in-time ICP-MS or GF-AAS elemental analysis techniques, incompatible with the logistical constraints of this experiment. Solutions were prepared by diluting the stock CA solutions with serum-free DMEM (1:10, 1:40, and 1:200 v/v). The cells were incubated 2 h with these solutions containing SPMnO, USPMnO, or MnCl_2 (2 mL per well; $n = 3$). The controls were incubated in serum-free DMEM ($n = 3$) and 90% DMEM with 10% nanopure water ($n = 3$). After incubation, the medium was removed and the cells were carefully rinsed five times with 1 mL of serum-free DMEM, followed by trypsinization (1 mL trypsin–EDTA 0.05% w/v from GIBCO; 5 min; 37 °C). The cells were collected in 2 mL of complete DMEM, and wells were rinsed with an equal volume of DMEM. The pooled cell suspension (~ 5 mL) was sedimented by centrifugation (500g, 5 min) and resuspended in 1 mL of serum-free DMEM. The cells were counted and assessed for viability with trypan blue (Cellometer automated cell counter, Nexcelom Bioscience, Lawrence, MA). A 500 μL aliquot of cell suspension was used for Mn cellular content measurement (see GF-AAS section). USPMnO and SPMnO-labeled cell suspensions were also sampled for TEM cell analysis. The remaining cell suspension were distributed in centrifugation tubes (500, 250, 100, and 50 μL) and pelleted (500g, 5 min) prior to MR imaging.

k. MRI Cell Pellet Imaging. MRI cell imaging was performed with a 1.0 T preclinical compact system (ASPECT Imaging, Netanya, Israel). The tubes containing the cell pellets were immersed in nanopure water and inserted in a 60 mm diameter whole-body rat coil for MR imaging. A T_1 -weighted 2D-spin echo sequence was used, with the following parameters: TE/TR = 9.6/718.5 ms; $\alpha = 90^\circ$; FOV = 60 mm; 1.0 mm slices, 400 \times 400; 3 excitations; 14 min acquisition time.

l. Transmission Electron Microscopy (TEM) Study. TEM was used to visualize the internalization of USPMnO and SPMnO particles into cells. For this, samples of the cell suspensions (100 μL) were fixed 24 h at 4 °C with 2.5% glutaraldehyde after treatment with 0.001 M sodium cacodylate buffer (pH 7.3). Then, they were stained with 0.5% uranyl acetate, dehydrated in a graded series of ethanol solutions, and embedded in Poly/Bed 812 epoxy (Polysciences Inc., Warrington, PA). Thin sections were processed and visualized at 120 keV TEM (Jeol-1230).

m. Image Treatment. To quantify the signal enhancement effect obtained with labeled cells, the reconstructed volume and the total intensity of each pellet were integrated with a routine developed with ImageJ (version 1.44, Wayne Rasband, National Institutes of Health, U.S.A.). Briefly, all the acquired slices were grouped in an image stack. The routine allowed the following steps: (1) a 20 pixels circular region of interest (ROI) was used to encircle each cell pellet, in each slice (1–3 slices per pellet); (2) for background subtraction, 30 \times 90 pixel ROIs were automatically generated between the tubes (in the water matrix), and the total signal of the water was integrated and averaged per pixel; (3) then, pixels in the circular ROI, corresponding to the cell pellet, were counted; their intensity (I_p) was integrated above a certain signal threshold, according to the following condition:

$$I_p > \bar{m}_b + C \times \text{std}_b$$

\bar{m}_b = mean intensity of background

std_b = standard deviation of background

$C = 0.4$ (correction factor)

RESULTS AND DISCUSSION

As-Synthesized MnO Nanocrystal Analysis. The nanocrystals synthesized in this study and used for relaxometric and cell labeling studies had narrow size distributions and mean diameters of 8.4 ± 0.8 nm (Figure 1). In parallel with the main

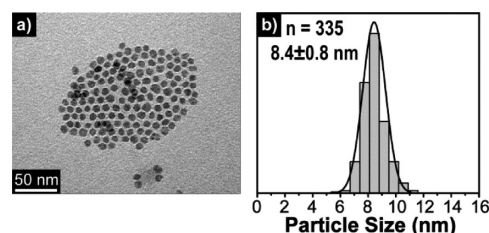


Figure 1. TEM image (120 keV) of (a) monodisperse MnO particles used for the relaxometric and cell labeling studies and (b) related particle-size distribution.

study, particles were also synthesized using variations to the heat ramp and to the precursor concentrations, which resulted in particles of mean diameters contained between 6.6 to 12.7 nm (SI, Figure S1b–d). MnO-oleate particles were suspended in chloroform and analyzed with DLS prior to ligand exchange. All particles appeared monodisperse ($0.07 < \sigma < 0.15$), except for the smallest particles (6.6 nm diam, synt. 4, see SI), which happened to be more difficult to purify from residual organic molecules. As small particles are expected to provide higher relaxometric properties, monodisperse nanoparticles showing the smallest particle size distribution were selected for the relaxometric and cell labeling studies (8.4 ± 0.8 nm diam). Both X-ray and electron diffraction measurements confirmed that MnO particles had a cubic structure (according to the International Center for Diffraction Data [ICDD; PDF No. 75-0257]). This is in agreement with results for MnO ultrasmall nanoparticles (see SI, Figure S2) and corresponds to a referenced density of 5.28 g/cm³.^{29,40,41}

MnO Particle Characterization and Stability Assays after Ligand Exchange. DMSA is a stable ligand in water over wide ranges of pH (from 3 to 11), in suitable ionic strengths (< 0.35 mol/L), and in various buffers.^{34,35,42} The carboxylic groups of DMSA bind to the metal oxide surface while providing disulfide bridges between the particle cores.³² Compared to dextran or starch coatings, DMSA-coated particles are anionic, and they are expected to strongly and nonspecifically interact with the cellular plasma membrane because of their negative surface charges.^{34,35}

A schematic representation of the coating procedure is provided in Figure 2a, whereas Figure 2b–d is TEM images illustrating the evolution of the nanoparticles through the coating procedure. As-synthesized MnO-oleate particles are well-ordered, with a thin coating (Figure 2b). However, upon coating with DMSA, the particles are covered by a thick layer of organic material, and it is more difficult to distinguish the boundaries of the oxide nanocores (Figure 2c). Further SPMnO TEM images are illustrated in the Supporting

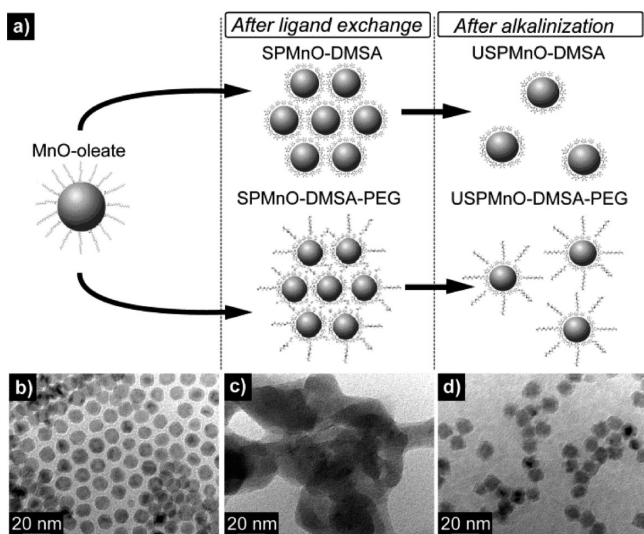


Figure 2. (a) Schematic representation of the different nanoparticle systems used in this study; TEM images of (b) MnO-oleate, (c) MnO-DMSA (SPMnO), and (d) MnO-DMSA-PEG (USPMnO, after alkalinization).

Information (Figures S3 and S4). The dimensions of ellipsoidal-shaped agglomerates (Figure S3) seem larger in TEM images (a 2-D imaging technique) and than results obtained with DLS (a 3-D measurement technique, see Table S1). SPMnO are susceptible to spread upon drying on the TEM grid; therefore, the mean diameter estimated in Figure S4 is not representative of the hydrodynamic diameter of particles in water. The excess of ligand appears to be largely eliminated following alkalinization and dialysis (Figure 2d). TEM images clearly revealed the strong difference in particle size after the individualization treatment, as well as evidenced the apparent elimination of ligands (DMSA) in excess from the particle surface.

The hydrodynamic diameters of aqueous suspensions of these particles were 17 nm for USPMnO nanoparticles, and 113 nm for SPMnO (Figure 3a). For USPMnO, hydrodynamic diameters larger than the crystal diameters (from TEM measurements) are expected, because of the presence of the ligand layer (DMSA and PEG) and the resulting hydrodynamic corona. Using PEG with DMSA resulted in lower hydrodynamic sizes for USPMnO (17 nm), compared with the use of DMSA only (26 nm; see Table S1, SI). This suggests that PEG has an impact on the elimination of DMSA from the particle coating. After alkalinization and dialysis in nanopure water, USPMnO suspensions are back to pH 6 (same as for SPMnO

suspensions). Thiol groups are negatively charged when deprotonated, and therefore, strong electrostatic repulsion occurs between DMSA-coated particles. Fauconnier et al. have observed the lack of reversibility of deprotonation in the pH range 3–11.³² Flocculation only occurs at very acidic pH, due to protonation of the free carboxylic functions only under such conditions. In the present study, we confirm these observations. We measured the zeta potential of USPMnO suspensions, and the results are presented in the Supporting Information (Figure S5). All products exhibit strongly negative zeta potentials under -20 mV, confirming the colloidal stability in a pH range 5–9. Finally, suspensions of MnO-DMSA and MnO-DMSA-PEG particles, dispersed in 154 mM NaCl, were stable for at least 7 days, without evidence of aggregation (Figure 3b,c). A slight increase of the hydrodynamic diameter was observed after 7 days, reflecting the possible cross-reaction of DMSA-coated particles through dithiol links or carboxylic interactions. Zeta potential measurements were performed with USPMnO at pH 5–9. The results are presented in Figure S5. Similar values were confirmed with SPMnO at near neutral pH (6.5). The stabilizing effect of DMSA coating on the colloidal stability was thereby confirmed (strongly negative zeta potentials).

Physico-Chemical Surface Analysis (XPS and FTIR).

XPS and FTIR analysis were performed on MnO-oleate, MnO-DMSA, and MnO-DMSA-PEG samples. Survey results are presented in Table 1 and high resolution spectra of C (1s) and O (1s) in Figure 4. The O/C ratios of MnO-oleate particles (0.301) were higher than the theoretical O/C ratio (0.111) expected for oleate only. The higher oxygen content was mainly attributed to MnO, thereby confirming the thinness of the oleate coating (TEM results, Figure 2b). Indeed, the analytical penetration depth of XPS is about 5 nm. For C (1s), the band at 285.0 eV (Figure 4) is attributed to $-C-C-$ and $-CH$; that at 286.6 eV to $-C-O-$; the one at 288.7 eV to $-COOH$. For O (1s), the band at 530.2 eV is attributed to metal–oxygen binding; that at 532.2 eV to $-C-O-$ and to one oxygen in $-COOH$; the one at 533.6 eV to the other oxygen in $-COOH$. FTIR spectra of MnO-oleate particles (Figure 5) revealed a significant contribution of CH vibration bands at 2922 and 2852 cm^{-1} (ν (CH_2), ν (CH_3)), unsaturations at 3007 cm^{-1} (ν ($\text{C}=\text{C}$)), and the presence of a band at 1730 cm^{-1} (ν_{COOH}). These bands are characteristic of the free carboxylic groups in the oleate structure.

Efficiency of Ligand Exchange from Oleate to DMSA or DMSA-PEG. FTIR did not reveal the presence of thiols (2561–2539 cm^{-1} in DMSA) nor $-S-S-$ bonds, most likely because disulfide links and thiols are more difficult to detect in FTIR than carboxylic groups. However, XPS surveys showed a

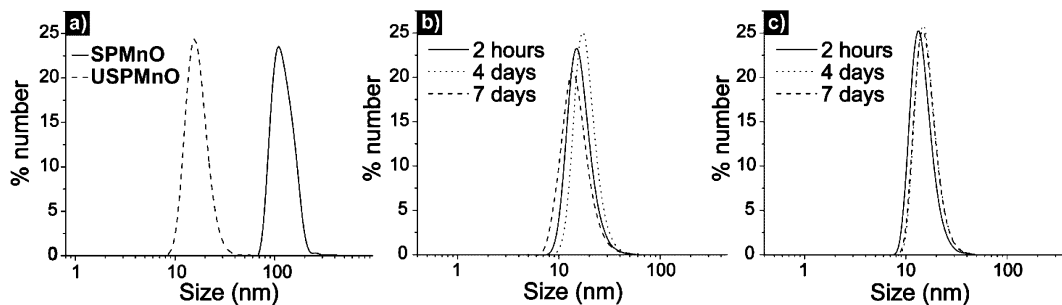


Figure 3. (a) MnO-DMSA-PEG DLS size-distribution of USPMnO (17 ± 5 d.nm) and SPMnO (113 ± 34 d.nm), both in nanopure water. Colloidal stability assay in saline (154 mM NaCl) for (b) USPMnO-DMSA and (c) USPMnO-DMSA-PEG.

Table 1. XPS Elemental Analysis of MnO Particles^a

particle or ligand	treatment ^b	C%	O%	S%	Mn%	O/C	S/C	S/Mn
MnO-oleate		67.7 ± 0.6	20.4 ± 0.3		4.6 ± 0.2	0.301		
MnO-DMSA	SPMnO	60.8 ± 0.1	24.1 ± 0.4	5.7 ± 0.4	5.3 ± 0.1	0.396	0.094	1.075
MnO-DMSA	USPMnO	45.5 ± 0.1	34.9 ± 0.3	5.7 ± 0.4	11.9 ± 0.1	0.767	0.125	0.479
MnO-DMSA-PEG	SPMnO	66.8 ± 5.8	20.6 ± 3.7	3.3 ± 1.7	2.5 ± 1.2	0.308	0.049	1.320
MnO-DMSA-PEG	USPMnO	57.8 ± 2.3	23.4 ± 1.8	2.1 ± 0.5	2.8 ± 0.8	0.405	0.036	0.750
DMSA (exp)		43.9 ± 0.1	39.0 ± 0.4	17.2 ± 0.3		0.888	0.441	
NH ₂ -PEG-SH (exp)		66.1 ± 0.2	33.6 ± 0.3	0.4 ± 0.1		0.508	0.006	

^aTheory: [oleate, C = 0.9, O = 0.1]; [DMSA, C = 0.4, O = 0.4, S = 0.2]; [NH₂-PEG-SH, C = 0.66, O = 0.33, S = 0.003]. ^bUSPMnO: alkalized; SPMnO: non-alkalinized.

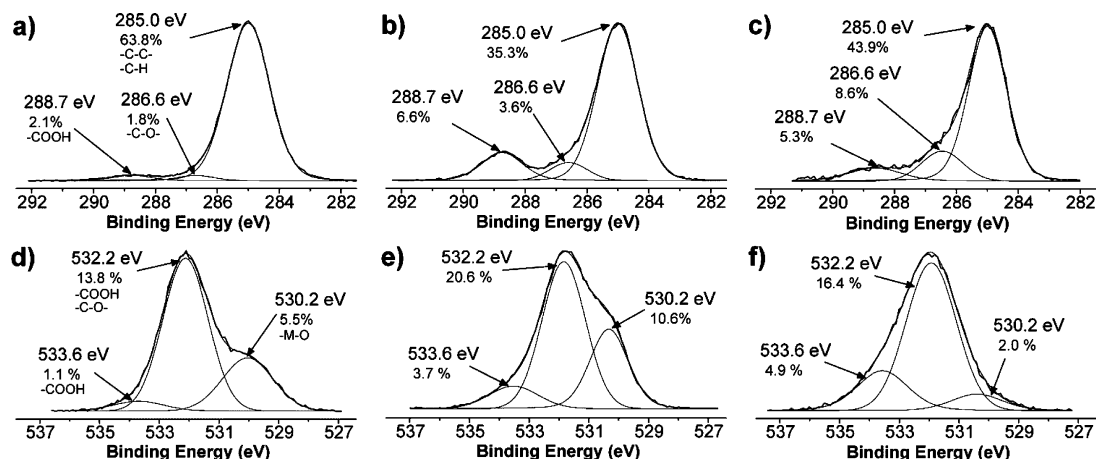


Figure 4. High-resolution XPS spectra of (a–c) C (1s) and (d–f) O (1s). (a, d) MnO-oleate, (b, e) MnO-DMSA (USPMnO), and (c, f) MnO-DMSA-PEG (USPMnO).

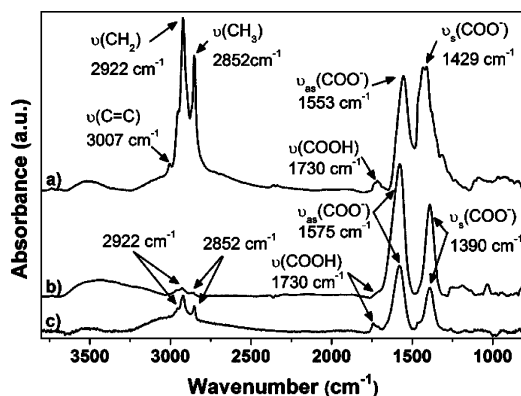


Figure 5. FTIR spectra of ligand exchange: (a) MnO-oleate, (b) MnO-DMSA (USPMnO), and (c) MnO-DMSA-PEG (USPMnO).

significant amount of sulfur for all products after ligand exchange, which confirmed the strong presence of DMSA around the particles. From FTIR, the bands at 3007, 2922, and 2852 cm⁻¹ of MnO-DMSA and MnO-DMSA-PEG spectra were much lower than those for MnO-oleate (Figure 5), indicating that oleate was largely eliminated from the nanoparticle surface. Assessment of ligand exchange was also clearly demonstrated by the shift of carbonyl bands. Asymmetric ($\nu_{\text{as}}(\text{COO}^-)$) and symmetric ($\nu_{\text{s}}(\text{COO}^-)$) carboxylate stretching bands at 1553 and 1429 cm⁻¹ initially present on the MnO-oleate spectrum, appeared shifted, respectively, at 1575 and 1390 cm⁻¹ on both MnO-DMSA and MnO-DMSA-PEG spectra. Using DMSA only for ligand exchange, instead of a combination of DMSA and PEG, seemed more efficient to

remove oleate away from the particle surface, as seen by the residual traces of oleate in specific bands around 2800 and 1730 cm⁻¹ (Figure 5c).

Characterization of DMSA Binding on MnO. The presence of carbonyl stretches confirmed that both DMSA and oleate were mainly bound to the metal oxide surface through carboxylate groups. The coordination type can be deduced from the wavenumber separation, Δ , between the $\nu_{\text{as}}(\text{COO}^-)$ and $\nu_{\text{s}}(\text{COO}^-)$ stretching bands: $\Delta > 200$ cm⁻¹ is monodentate, $\Delta < 120$ cm⁻¹ is bidentate, and $140 < \Delta < 200$ cm⁻¹ corresponds to a bridging ligand.⁴³ The oleate coating appeared bidentate for MnO-oleate ($\Delta = 124$ cm⁻¹) and bridged for MnO-DMSA and MnO-DMSA-PEG ($\Delta = 185$ cm⁻¹).

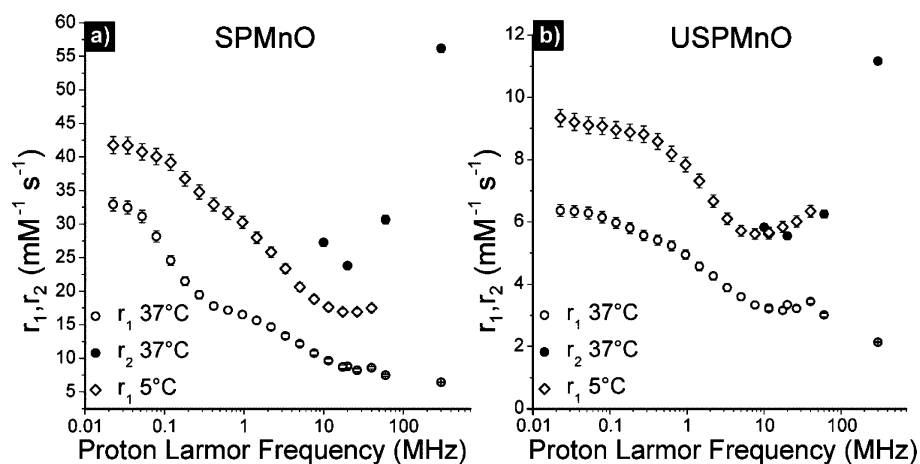
Confirmation of PEG Grafting. XPS survey spectra clearly evidenced the higher carbon components in MnO-DMSA-PEG compared with MnO-DMSA (57.8–45.5%, Table 1). Similarly, the percentage of Mn was lower, leading to a higher S/Mn ratio for MnO-DMSA-PEG. Furthermore, the characteristic peak of O (1s) from the metal oxide contribution (~ 530 eV) decreased from 10.4% (MnO-DMSA) to 1.6% (MnO-DMSA-PEG). These observations indicate a denser coating layer on MnO-DMSA-PEG (lower %Mn) and richer in C, coming from either PEG grafting or from residual oleate. However, C (1s) HR-XPS spectra (Figure 4) indicated a high relative contribution (8.6%) of PEG-related $-\text{C}-\text{O}-$ links (286.6 eV) for MnO-DMSA-PEG particles, 5% up from MnO-DMSA particles, and 6.8% up from MnO-oleate. This demonstrates the presence of PEG around MnO-DMSA-PEG particles.

Impact of Alkalinization. Finally, the individualization of particles after alkalinization treatment (from SPMnO to

Table 2. Size and Relaxation Properties of MnO-DMSA-PEG Suspensions Used for Cell Labeling Experiments (60 MHz, 20 °C)

contrast agent	core diameter ^a (nm)	hydrodynamic diameter ^b (nm)	T_1^c (ms)	r_1 (mM ⁻¹ s ⁻¹)	r_2 (mM ⁻¹ s ⁻¹)	r_2/r_1
SPMnO-DMSA-PEG	8.4 ± 0.8	113 ± 34	78.1 ± 0.2	17.0 ± 0.5	68.5 ± 2.1	4.0
USPMnO-DMSA-PEG	8.4 ± 0.8	17 ± 5	83.3 ± 0.2	3.4 ± 0.1	11.0 ± 0.3	3.2
Mn ²⁺			80.7 ± 0.2	6.1 ± 0.2	66.1 ± 2.0	10.9

^aCore diameter was determined by TEM; FWHM of the size distribution used as the error. ^bHydrodynamic diameter measured by DLS at 25 °C (number); FWHM of the size distribution used as the error. ^cMean on triplicate with the standard deviation used as the error.

**Figure 6.** NMRD profiles of (a) SPMnO and (b) USPMnO performed at 5 and 37 °C.

USPMnO) lead to a reduction of the organic coating, as clearly indicated by the decrease in C contribution and higher Mn contents (Table 1).⁴⁴ When DMSA-coated metal oxide nanoparticles are dispersed in alkaline water, one of the two carboxylic groups spontaneously unlinks from the nanoparticle surface.^{32,45} Under these conditions, carboxylic groups (COOH) deprotonate into carboxylates (COO⁻), providing therefore enough negative charge to stabilize the colloids via electrostatic repulsion, and freeing thereby a significant amount of DMSA from the coating. As previously mentioned, reprotonation only occurs at acidic pH (<3).

Relaxometric Characterization at 60 MHz (1.41 T). No study has reported so far the influence of agglomeration on the relaxometric properties of MnO nanoparticle suspensions. The relaxivity is defined as the inverse of the relaxation time, normalized to the concentration of paramagnetic element; it is calculated from the slope of $1/T_{i(1,2)}$ plotted against [Mn]. In the present study, the relaxivity was calculated using molar ionic concentrations, which allows for direct comparisons with relaxivity values of the ion Mn²⁺, as well as with Mn chelates used as contrast agents. Because Mn is toxic at high concentrations, molar relativities are crucial for estimating local toxicological risks to cells and tissues exposed to high levels of Mn. The molar longitudinal relaxivities (r_1) measured for SPMnO suspensions appeared much higher than their USPMnO counterparts (Table 2; $r_1 = 3.4$ mM⁻¹s⁻¹ for USPMnO and $r_1 = 17.0$ mM⁻¹s⁻¹ for SPMnO). These values are higher than previously reported values for 7 nm core size MnO particles (0.37 mM⁻¹s⁻¹ at 3 T) and 18 nm core size MnO (0.353 mM⁻¹s⁻¹ at 1.5 T).²⁹ Park et al. recently reported $r_1 = 7.02$ mM⁻¹s⁻¹ at 1.5 T for 2–3 nm diameter glucuronic acid-coated particles.³⁰ Although the longitudinal relaxivities obtained for individual particles in the present study were smaller, the r_2/r_1 relaxometric ratio was closer to unity ($r_2/r_1 = 3.2$ compared to $r_2/r_1 = 6.83$ for glucuronic acid-coated MnO). Reaching relaxometric ratios ideally under values of 3–4 is

essential in order to preserve strong signal enhancement properties, resulting in positive contrast in MRI (SI, Figure S6).⁴⁶ In this study, the relaxometric ratios of SPMnO and USPMnO suspensions, 4.0 and 3.2 respectively, are clearly different from the values obtained with Mn²⁺ ions (10.9).

Mn²⁺ exhibits an anomalous relaxation behavior due to the isotropic “contact” interaction between the electron spin of Mn²⁺ and protons in the first hydration shell.^{47,48} Mn²⁺ behaves differently from other paramagnetic ions, mainly at low fields. The electronic wave function of hydrated Mn²⁺ ions is delocalized and a significant amount of its spin extends to the water protons of the first hydration shell.⁴⁹ The contact interaction does not affect T_1 at MR imaging field strengths but does shorten T_2 . In the case of Mn chelates (e.g., Mn-EDTA), the absence of a contact interaction, explained by the drastic reduction of water molecules in the first coordination layer of the CA, results in r_2/r_1 ratios in the order of 2–3.⁵⁰ The r_2/r_1 values for SPMnO and USPMnO are 4 and 3.2, respectively (Table 2). Therefore, the performance of MnO-DMSA-PEG particles as “positive” CAs does not appear significantly impeded by agglomeration and appears close to that of Mn chelates. The density of cubic MnO structure is 5.28 g/cm³ (International Center for Diffraction Data, ICDD). A 8.4 nm diameter MnO nanocrystal, with a unit volume of 310 nm³, should contain in the order of 1.4×10^4 Mn atoms. From Figure 2d, the total mean diameter of DMSA and PEG-coated particles is estimated to about 10 nm. Therefore, a spherical 100 nm SPMnO nanoparticle would theoretically contain about 1000 USPMnO particles. Although not precisely measurable, the relaxivity per particle is therefore expected to reach very high values.

Relaxometric Characterization at Varying Magnetic Field Strengths. According to the water and methanol test, exchangeable protons in both SPMnO and USPMnO suspensions relax at higher rates than nonexchangeable protons, meaning that water protons relax according to an inner sphere

model (data not shown).³⁹ The relaxometric principles for this model are presented in the Appendix included in the Supporting Information. Figure 6a,b shows the NMRD profile of SPMnO and USPMnO at 5 and 37 °C, as well as r_2 values. First, the longitudinal relaxivity (r_1) of SPMnO was higher than for USPMnO at every magnetic field, about 3 to 4 times at fields <1 MHz. Then, SPMnO r_1 profiles displayed sigmoid-shaped curves with two inflections: one at low magnetic field strengths (<1 MHz) and one at medium field strengths (between 1 and 10 MHz). For USPMnO, only the inflection at medium field strengths was clearly evidenced. The dispersion at low magnetic field strengths observed for SPMnO (Figure 6a) is referred to as “scalar” or “hyperfine” and corresponds to the term $1/T_{1M}^{SC}$ in (eqs 2 and 3 in the Appendix, SI). This “contact” interaction at ~0.1 MHz is attributed to the presence of Mn^{2+} ions in the solutions.⁴⁹ In the present study, MnO particles had been thoroughly washed before coating with DMSA and PEG, then rinsed, then dialyzed and finally immediately characterized for relaxometric properties. Therefore, the amount of residual Mn^{2+} ions is expected to be low. However, the low-field dispersion seen in SPMnO NMRD profiles could be attributed in part to residual Mn^{2+} ions complexed with DMSA, in excess for SPMnO-DMSA-PEG. These ions are seemingly eliminated from the CAs upon alkalization, as confirmed by the absence of a low-field dispersion in USPMnO NMRD curves (Figure 6b).

The second inflection, appearing between 1 and 10 MHz for both SPMnO and USPMnO, is qualitatively consistent with the mechanisms of proton relaxation by dipolar interactions between the coordinated water protons and the paramagnetic ions. This inflection is widely observed in paramagnetic complexes, such as with EDTA or DTPA.⁵¹ In each paramagnetic contrast agent system and at every magnetic field strength, only one correlation time controls the contributive factor $1/\tau_{ci}$ (eq 6 in the Appendix, SI) and, in turn, the relaxivity: the rotational time of the paramagnetic element (τ_R), which corresponds to the reorientation of the metal-proton vector, the exchange time between solvent protons and protons in the close vicinity of manganese (τ_M) and the electronic relaxation time of manganese (τ_{si}). In the inner-sphere relaxation mechanism model, the dipolar interaction is modulated by the smallest of the three correlation times (eq 6 in the Appendix, SI). The scalar interaction is modulated by τ_M and τ_{s2} (eq 4 in the Appendix, SI).

The NMRD curves measured for both SPMnO and USPMnO, at 5 and 37 °C, provide evidence of a contribution from the three factors (τ_R , τ_M , τ_{si}). First, for large molecules and nanoparticles, the reorientation of the metal-proton vector is expected to be relatively slow (long τ_R), therefore, τ_R is not expected to be the main limiting factor guiding $1/\tau_{ci}$. Then, both SPMnO and USPMnO suspensions measured at 5 °C resulted in higher relaxivities than at 37 °C. This is an indication that τ_{si} is not the only contributing factor, because temperature mainly affects τ_R and τ_M through modulation of the viscosity and exchange rates in the solvent. At low field, relaxivities of USPMnO suspensions do vary approximately linearly with η/T ; this is an indication that the correlation time is influenced by the rotational motion.⁵² Although difficult to quantify, the specific contribution of τ_R to the relaxivity of SPMnO, directly influenced by its larger diameter, certainly has a significant contribution on the higher observed relaxivities. Also, as expected, the presence of DMSA and highly hydrophilic PEG as a surface coating, preserve water

accessibility and exchange with Mn ions. This is a very important factor contributing to high longitudinal relaxivities. The correlation time for each curve can be estimated from the frequency at the inflection point of the dipolar dispersion, a condition for which $\omega_s \tau_{c2} = 1$. For SPMnO and USPMnO at 37 °C, the inflection point occurs at ~2.5 MHz. Because $\omega_s \cong 1.04 \times 10^{10} \text{ s}^{-1}$ at this field, $\tau_c \cong 9.6 \times 10^{-10} \text{ s}$. Therefore, it is likely that electron spin relaxation makes a significant contribution to shorten the observed correlation time. The slight upward turn of all curves in the high-field region (20–30 MHz) indicates that electronic relaxation time, increasing with the magnetic field strength, could be an important limiting factor in that range. Finally, for both SPMnO and USPMnO measured at 37 °C, the decrease of relaxivity above 50 MHz is attributed to dipolar dispersion ($\omega_s \tau_c$).

The transversal relaxivities were measured at 37 °C and are also plotted in Figure 6a,b (full circles). At high fields, the sharp increase of r_2 is attributed to the higher magnetic moment of the particles. At high fields, the relative increase of r_2 is much higher for SPMnO than for USPMnO (r_2/r_1 of 8.7 and 5.3, respectively). This indicates that agglomeration and, therefore, susceptibility effects, contribute to the transversal relaxation times more than scalar interactions of Mn at magnetic fields higher than 3 T. The comprehensive characterization and detailed understanding of the mechanisms of hydrogen proton relaxation in the presence of ultrasmall manganese oxide nanocrystals would require further analysis. However, this study shows evidence that such systems present interesting relaxometric properties that can be optimized and exploited in MRI applications.

MRI Visualization. Tubes containing dilutions of SPMnO-DMSA-PEG were visualized at 1.5 T in T_1 -weighted spin echo sequences (Figure 7). The suspensions appeared bright, with a

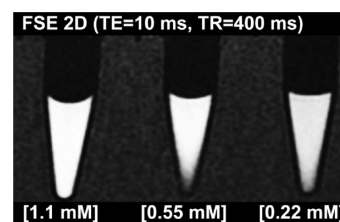


Figure 7. Dilutions of DMSA-PEG-coated SPMnO imaged with a T_1 -weighted MRI spin echo sequence.

maximum intensity at 1.1 mM. This maximum, as well as corresponding T_1 values at this concentration, is in agreement with the equation of signal for the spin echo sequence (SI, Figure S6).

Cell Labeling. SPMnO and USPMnO-DMSA-PEG were used to label HT-1080 cancer cells. The cells were incubated (2 h) with high concentrations of CA, then thoroughly washed, harvested, and pelleted. Cells labeled with SPMnO and USPMnO clearly appeared positively contrasted for Mn concentrations above 0.9 pg Mn/cell (Figure 8a,b). Based on our observations, a minimum Mn incubation concentration of ~2 mg/L is necessary for SPMnO to reach minimum detection thresholds in T_1 -weighted MRI. For USPMnO, this concentration is ~6 mg/L (Figures 8 and 10a). At such incubation conditions, we observed Mn cell uptake in the order of ~0.6–0.8 and ~0.3–0.6 pg Mn/cell for SPMnO and USPMnO, respectively. For Mn^{2+} ions, the detection threshold was lower (<0.9 pg/cell, Figure 8c). The minimum number of SPMnO-

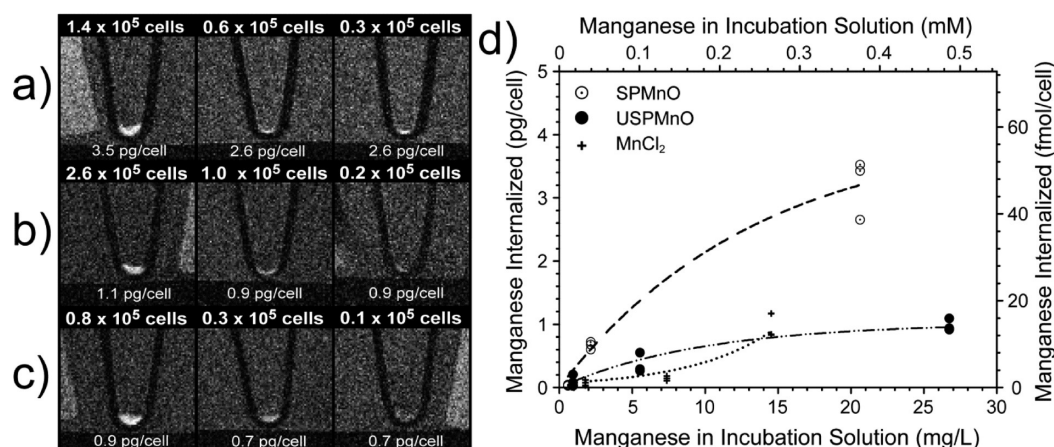


Figure 8. T_1 -weighted MR images of HT-1080 cells labeled with (a) SPMnO (0.38 mM), (b) USPMnO (0.49 mM), and (c) Mn^{2+} (0.27 mM). The numbers under each pellet indicate the mass of Mn detected per cell. (d) Mn uptake in labeled cells, depending on the concentration of Mn in the incubation media.

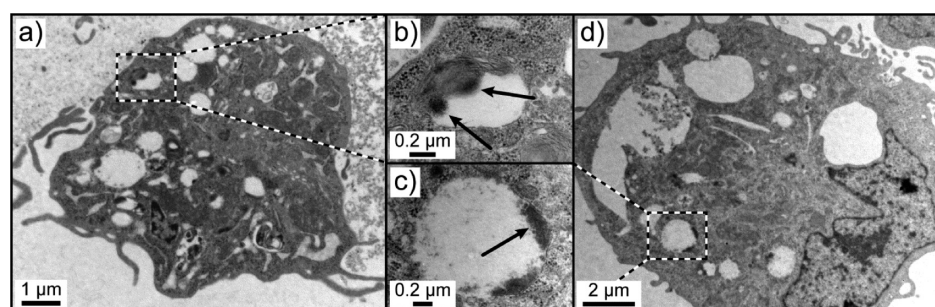


Figure 9. TEM of HT-1080 cells incubated with SPMnO (a, b) and with USPMnO (c, d).

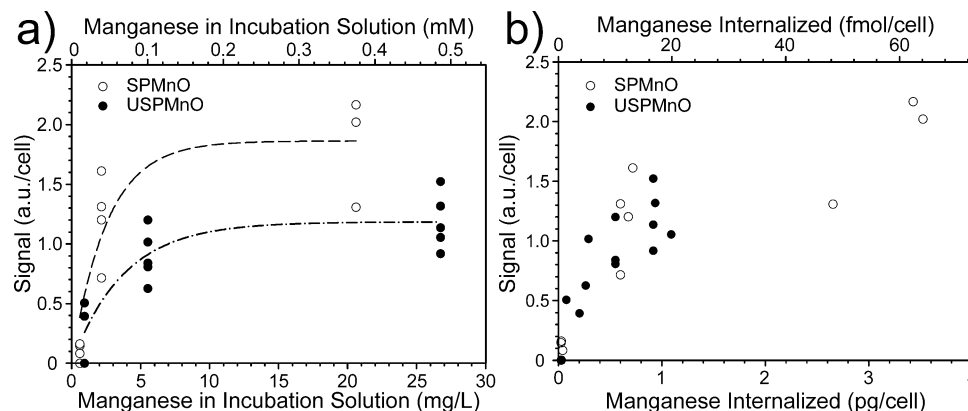


Figure 10. Effect of Mn concentration in incubation media on the total signal detected per cell.

labeled cells visualized in MRI was 30000 in 1 mm thick slices. Using thinner slices (0.5 mm) could significantly improve the detection limit and the minimum number of detected cells by reducing the partial volume effect.

After 2 h of incubation, higher amounts of manganese were taken up with SPMnO compared to USPMnO (Figure 8d). Uptake of Mn^{2+} ions was lower than for particles, and showed evidence of an ion pump-mediated mechanism.^{53,54} However, the viability of Mn^{2+} -labeled cells was not preserved at incubation concentrations of 0.26 mM and higher (SI, Table S2). In fact, the cells labeled in this study were submitted to relatively high concentrations of Mn, and the cell viability was best preserved by using USPMnO (individual particles). USPMnO did not affect the viability of cells up to 0.49 mM

Mn, whereas both significant inflection in viability and decrease in number of cells were noted for an incubation treatment of 0.38 mM Mn with SPMnO (SI, Table S2). Therefore, the use of USPMnO is preferable to maintain high Mn cell labeling efficiency without affecting cell proliferation and viability. Finally, these results suggest that incubation with $MnCl_2$ is susceptible to affect both the proliferation and the viability of cells as robust as HT-1080 for concentrations necessary to reach T_1 -weighted MRI detection thresholds.

Transmission Electron Microscopy (TEM) Study. As confirmed by TEM, both SPMnO and USPMnO nanoparticles are ingested in the endosomes (Figure 9). However, there were clear differences in the endosomal distribution of particles between SPMnO and USPMnO. First, SPMnO of size

corresponding to the hydrodynamic diameter of the nano-aggregates were found in the endosomes (Figures 9a,b and S7). Identification of at least 12 cases of SPMnO nanoparticles entrapped in the endosomes confirmed that SPMnO in endosomes form 200 ± 10 nm aggregates (average on 12 particles, 24 diameter values measured). USPMnO (Figure 9c,d) also appeared as aggregates, suggesting that particles agglomerate upon retention in the endosomes. These results suggest that both products are internalized by endocytosis, most likely enhanced by the DMSA coating, as suggested by previous work on DMSA-coated iron oxide particles.^{34,35} The high efficiency of anionic particles uptake is related to the nonspecific nanoparticles absorption on the cell membrane.³⁵

Quantification of MRI Signal in the Labeled Cell Pellets. The signal per cell was clearly higher for SPMnO-labeled, compared with USPMnO-labeled cells (Figure 10a). Both products reached a plateau in signal intensity per cell for incubation concentrations of about 0.1–0.2 mM Mn. The higher signal per cell is clearly correlated to the total amount of internalized Mn (Figure 10b). However, no significant difference was found in the total signal per cell, for USPMnO and SPMnO-labeled cells having ingested similar quantities of Mn. Although internalization is more efficient with nano-agglomerates (SPMnO), both contrast agents provide the same signal-enhancement effect per Mn atom, in accordance with their similar r_2/r_1 ratio. In summary, although suspensions of MnO particles in the form of agglomerates reach higher relaxivities, once these are ingested by cells, their MR signal enhancement efficiency, as measured with T_1 -weighted MRI, is not higher than that obtained for USPMnO (Figure 10b). This difference is most possibly due to the fact that USPMnO agglomerate in the cell's endosomes upon internalization (Figure 9c), resulting in a similar "state" of labeling compared with SPMnO. However, SPMnO labeling is more efficient in terms of Mn internalization rate, while preserving the viability at Mn incubation concentrations <0.38 mM.

CONCLUSION

Agglomeration has a limited impact on the MR signal-enhancement properties of aqueous suspensions of DMSA- and DMSA-PEG-coated MnO nanoparticles used in cell labeling applications. Coating the particles with DMSA allows efficient nanoparticle internalization, while preserving the cell viability. Relaxometric ratios (r_2/r_1) in the same order were found for agglomerates and individual particles. Although agglomerates were more efficiently internalized by HT-1080 cells, no clear difference in signal was measured between USPMnO and SPMnO-labeled cells at similar concentrations of Mn per cell. Compared with iron oxide particle suspensions for which agglomeration in aqueous media results in large differences of relaxometric ratios and drastic decrease of signal intensity, suspensions of MnO particles preserve their MR signal enhancement properties upon agglomeration. These properties could be exploited in the perspective of more quantitative cell labeling and tracking applications with MRI, using more complex cell cultures such as stem cells, Langerhans Islets, as well as immune cells.

ASSOCIATED CONTENT

Supporting Information

Variations to the primary synthesis, XRD analysis, simulated MR signal intensity, supplementary data related to cell labeling studies, and an appendix on theoretical consideration of

relaxometry. This material is available free of charge via the Internet at <http://pubs.acs.org>.

AUTHOR INFORMATION

Corresponding Author

*Phone: (418) 656-2131, ext. 8682. Fax: (418) 656-5343. E-mail: marc-andre.fortin@gmn.ulaval.ca.

Author Contributions

[†]Equal contributors to this work.

Notes

The authors declare no competing financial interest.

ACKNOWLEDGMENTS

The authors acknowledge the valuable contributions of A. Hocq (NMRD measurements), Richard Janvier (TEM work), and Sandra Deschênes (MRI work at CHUQ) to this work. This study was supported by NSERC (Canada), FRSQ, and FQRNT (Québec).

REFERENCES

- (1) Kort, H. D. *Br. Med. J.* **2011**, *342*, 426.
- (2) Corot, C.; Robert, P.; Idee, J. M.; Port, M. *Adv. Drug Delivery Rev.* **2006**, *58*, 1471.
- (3) Bulte, J. W. M. *Am. J. Roentgenol.* **2009**, *193*, 314.
- (4) Wang, Y. X. J.; Hussain, S. M.; Krestin, G. P. *Eur. Radiol.* **2001**, *11*, 2319.
- (5) Weissleder, R.; Cheng, H. C.; Bogdanova, A.; Bogdanov, A. J. *Magn. Reson. Imagin* **1997**, *7*, 258.
- (6) de Vries, I. J. M.; Lesterhuis, W. J.; Barentsz, J. O.; Verdijk, P.; van Krieken, J. H.; Boerman, O. C.; Oyen, W. J. G.; Bonenkamp, J. J.; Boezeman, J. B.; Adema, G. J.; Bulte, J. W. M.; Scheenen, T. W. J.; Punt, C. J. A.; Heerschap, A.; Figdor, C. G. *Nat. Biotechnol.* **2005**, *23*, 1407.
- (7) Zhu, J.; Zhou, L.; XingWu, F. N. *Engl. J. Med.* **2006**, *355*, 2376.
- (8) Callera, F.; Melo, C. M. T. P. *Stem Cells Dev.* **2007**, *16*, 461.
- (9) Toso, C.; Valle, J. P.; Morel, P.; Ris, F.; Demuylder-Mischler, S.; Lepetit-Coiffe, M.; Marangon, N.; Saudek, F.; Shapiro, A. M. J.; Bosco, D.; Berney, T. *Am. J. Transplant.* **2008**, *8*, 701.
- (10) Rogers, W. J.; Meyer, C. H.; Kramer, C. M. *Nat. Clin. Pract. Cardiovasc. Med.* **2006**, *3*, 554.
- (11) Metz, S.; Bonaterra, G.; Rudelius, M.; Settles, M.; Rummeny, E. J.; Daldrup-Link, H. E. *Eur. Radiol.* **2004**, *14*, 1851.
- (12) Muller, R. N.; Vander Elst, L.; Roch, A.; Peters, J. A.; Csajbok, E.; Gillis, P.; Gossuin, Y. *Adv. Inorg. Chem.* **2005**, *57*, 239.
- (13) Daldrup-Link, H. E.; Rudelius, M.; Oostendorp, R. A.; Jacobs, V. R.; Simon, G. H.; Gooding, C.; Rummeny, E. J. *Acad. Radiol.* **2005**, *12*, 502.
- (14) Bulte, J. W. M.; Kraitchman, D. L. *NMR Biomed.* **2004**, *17*, 484.
- (15) Weissleder, R.; Stark, D. D.; Engelstad, B. L.; Bacon, B. R.; Compton, C. C.; White, D. L.; Jacobs, P.; Lewis, J. *Am. J. Roentgenol.* **1989**, *152*, 167.
- (16) Weissleder, R.; Elizondo, G.; Wittenberg, J.; Lee, A. S.; Josephson, L.; Brady, T. J. *Radiology* **1990**, *175*, 494.
- (17) Crich, S. G.; Biancone, L.; Cantaluppi, V.; Esposito, D. D. G.; Russo, S.; Camussi, G.; Aime, S. *Magn. Reson. Med.* **2004**, *51*, 938.
- (18) Nolte, I. S.; Gungor, S.; Erber, R.; Plaxina, E.; Scharf, J.; Misselwitz, B.; Gerigk, L.; Przybilla, H.; Groden, C.; Brockmann, M. A. *Magn. Reson. Med.* **2008**, *59*, 1014.
- (19) Modo, M.; Mellodew, K.; Cash, D.; Fraser, S. E.; Meade, T. J.; Price, J.; Williams, S. C. R. *Neuroimage* **2004**, *21*, 311.
- (20) Vu, K.; Xie, J. W.; McDonald, M. A.; Bernardo, M.; Hunter, F.; Zhang, Y. T.; Li, K.; Bednarski, M.; Guccione, S. *Bioconjugate Chem.* **2005**, *16*, 995.
- (21) Gilad, A. A.; Walczak, P.; McMahon, M. T.; Na, H. B.; Lee, J. H.; An, K.; Hyeon, T.; van Zijl, P. C.; Bulte, J. W. *Magn. Reson. Med.* **2008**, *60*, 1.

- (22) Faucher, L.; Guay-Bégin, A.-A.; Lagueux, J.; Côté, M.-F.; Petitclerc, É.; Fortin, M.-A. *Contrast Media Mol. Imaging* **2011**, 6, 209.
- (23) Lauterbur, P. C. *Nature* **1973**, 242, 190.
- (24) Aoki, I.; Takahashi, Y.; Chuang, K. H.; Silva, A. C.; Igarashi, T.; Tanaka, C.; Childs, R. W.; Koretsky, A. P. *NMR Biomed.* **2006**, 19, 50.
- (25) Yamada, M.; Gurney, P. T.; Chung, J.; Kundu, P.; Drukker, M.; Smith, A. K.; Weissman, I. L.; Nishimura, D.; Robbins, R. C.; Yang, P. C. *Magn. Reson. Med.* **2009**, 62, 1047.
- (26) Winter, P. M.; Neubauer, A. M.; Caruthers, S. D.; Harris, T. D.; Robertson, J. D.; Williams, T. A.; Schmieder, A. H.; Hu, G.; Allen, J. S.; Lacy, E. K.; Zhang, H. Y.; Wickline, S. A.; Lanza, G. M. *Arterioscler., Thromb., Vasc. Biol.* **2006**, 26, 2103.
- (27) Sirol, M.; Itskovich, V. V.; Mani, V.; Aguinaldo, J. G.; Fallon, J. T.; Misselwitz, B.; Weinmann, H. J.; Fuster, V.; Toussaint, J. F.; Fayad, Z. A. *Circulation* **2004**, 109, 2890.
- (28) Frias, J. C.; Williams, K. J.; Fisher, E. A.; Fayad, Z. A. *J. Am. Chem. Soc.* **2004**, 126, 16316.
- (29) Na, H. B.; Lee, J. H.; An, K.; Park, Y. I.; Park, M.; Lee, I. S.; Nam, D. H.; Kim, S. T.; Kim, S. H.; Kim, S. W.; Lim, K. H.; Kim, K. S.; Kim, S. O.; Hyeon, T. *Angew. Chem., Int. Ed.* **2007**, 46, 5397.
- (30) Park, J. Y.; Choi, E. S.; Baek, M. J.; Lee, G. H.; Woo, S.; Chang, Y. *Eur. J. Inorg. Chem.* **2009**, 2477.
- (31) Fortin, M. A.; Tremblay, M.; Lagueux, J.; Létourneau, M.; Faucher, L.; Rojas, D. *Proc. Intl. Soc. Mag. Reson. Med.* **2011**, 19, #3708.
- (32) Fauconnier, N.; Pons, J. N.; Roger, J.; Bee, A. J. *Colloid Interface Sci.* **1997**, 194, 427.
- (33) Auffan, M.; Decome, L.; Rose, J.; Orsiere, T.; De Meo, M.; Briois, V.; Chaneac, C.; Olivi, L.; Berge-LeFranc, J. L.; Botta, A.; Wiesner, M. R.; Bottero, J. Y. *Environ. Sci. Technol.* **2006**, 40, 4367.
- (34) Billotey, C.; Wilhelm, C.; Devaud, M.; Bacri, J. C.; Bittoun, J.; Gazeau, F. *Magn. Reson. Med.* **2003**, 49, 646.
- (35) Wilhelm, C.; Billotey, C.; Roger, J.; Pons, J. N.; Bacri, J. C.; Gazeau, F. *Biomaterials* **2003**, 24, 1001.
- (36) Golander, C. G.; Herron, J. N.; Lim, K.; Claesson, P.; Andrade, J. D. In *Poly(ethylene glycol) chemistry: biotechnical and biomedical applications*; Harris, J. M., Ed. Plenum Press: New York, 1992, p 221.
- (37) Park, J.; An, K. J.; Hwang, Y. S.; Park, J. G.; Noh, H. J.; Kim, J. Y.; Park, J. H.; Hwang, N. M.; Hyeon, T. *Nat. Mater.* **2004**, 3, 891.
- (38) NIH; rsbweb.nih.gov/ij.
- (39) Gossuin, Y.; Roch, A.; Muller, R. N.; Gillis, P. J. *Magn. Reson.* **2002**, 158, 36.
- (40) Lee, G. H.; Huh, S. H.; Jeong, J. W.; Choi, B. J.; Kim, S. H.; Ri, H. C. *J. Am. Chem. Soc.* **2002**, 124, 12094.
- (41) Seo, W. S.; Jo, H. H.; Lee, K.; Kim, B.; Oh, S. J.; Park, J. T. *Angew. Chem., Int. Ed.* **2004**, 43, 1115.
- (42) Chen, Z. P.; Zhang, Y.; Zhang, S.; Xia, J. G.; Liu, J. W.; Xu, K.; Gu, N. *Colloids Surf., A* **2008**, 316, 210.
- (43) Nakamoto, K. *Infrared and Raman Spectra of Inorganic and Coordination Compounds*, 5th ed.; Wiley: New York, 1997, Part B, p 59.
- (44) Valois, C. R. A.; Braz, J. M.; Nunes, E. S.; Vinolo, M. A. R.; Lima, E. C. D.; Curi, R.; Kuebler, W. M.; Azevedo, R. B. *Biomaterials* **2010**, 31, 366.
- (45) Roca, A. G.; Veintemillas-Verdaguer, S.; Port, M.; Robic, C.; Serna, C. J.; Morales, M. P. *J. Phys. Chem. B* **2009**, 113, 7033.
- (46) Faucher, L.; Gossuin, Y.; Hocq, A.; Fortin, M. A. *Nanotechnology* **2011**, 22, 295103.
- (47) Bernheim, R. A.; Brown, T. H.; Gutowsky, H. S.; Woessner, D. E. *J. Chem. Phys.* **1959**, 30, 950.
- (48) King, J.; Davidson, N. J. *Chem. Phys.* **1958**, 29, 787.
- (49) Koenig, S. H.; Brown, R. D., 3rd. *Magn. Reson. Med.* **1984**, 1, 478.
- (50) Vymazal, J.; Bulte, J. W.; Frank, J. A.; Di Chiro, G.; Brooks, R. A. *J. Magn. Reson. Imaging* **1993**, 3, 637.
- (51) Koenig, S. H.; Baglin, C.; Brown, R. D., 3rd; Brewer, C. F. *Magn. Reson. Med.* **1984**, 1, 496.
- (52) Bertini, I.; Luchinat, C. *NMR of Paramagnetic Molecules in Biological Systems*; Benjamin/Cummings Pub. Co.: Menlo Park, CA, 1986.
- (53) Narita, K.; Kawasaki, F.; Kita, H. *Brain Res.* **1990**, 510, 289.
- (54) Durr, G.; Strayle, J.; Plemper, R.; Elbs, S.; Klee, S. K.; Catty, P.; Wolf, D. H.; Rudolph, H. K. *Mol. Biol. Cell* **1998**, 9, 1149.